High-Safety Electrolytes for Lithium-Ion Batteries

Is non-flammability of electrolyte overrated in the overall safety performance of lithium ion batteries?

September 2022

Wu Xu
Hao Jia
Lirong Zhong
Xia Cao

DISCLAIMER

This report was prepared as an account of work sponsored by an agency of the United States Government. Neither the United States Government nor any agency thereof, nor Battelle Memorial Institute, nor any of their employees, makes **any warranty, express or implied, or assumes any legal liability or responsibility for the accuracy, completeness, or usefulness of any information, apparatus, product, or process disclosed, or represents that its use would not infringe privately owned rights**. Reference herein to any specific commercial product, process, or service by trade name, trademark, manufacturer, or otherwise does not necessarily constitute or imply its endorsement, recommendation, or favoring by the United States Government or any agency thereof, or Battelle Memorial Institute. The views and opinions of authors expressed herein do not necessarily state or reflect those of the United States Government or any agency thereof.

High-Safety Electrolytes for Lithium-Ion Batteries

Is non-flammability of electrolyte overrated in the overall safety performance of lithium ion batteries?

September 2022

Wu Xu
Hao Jia
Lirong Zhong
Xia Cao

Prepared for
the U.S. Department of Energy
under Contract DE-AC05-76RL01830

Pacific Northwest National Laboratory
Richland, Washington 99354

Abstract

It has been widely considered that the flammability of the liquid electrolyte is one of the most influential factors that determine the safety of lithium ion batteries (LIBs). Following this consideration, a completely non-flammable electrolyte was designed and adopted to graphite‖LiFePO$_4$ (Gr‖LFP) batteries. Contrary to the conventional understanding, the completely non-flammable electrolyte with phosphorus-containing solvents exhibits inferior safety performance in commercial Gr‖LFP batteries, in comparison to the flammable conventional LiPF$_6$-organocarbonate electrolyte. Mechanistic studies identify the exothermic reactions between the electrolyte (especially the flame retarding phosphate solvent) and the charged electrodes as the "culprit" behind such a counterintuitive phenomenon. The discovery emphasizes the importance of reducing the electrolyte reactivity when designing safe electrolytes, as well as the necessity of evaluating safety performances of electrolyte on a battery level.

Summary

For the first time, a rigorously non-flammable LHCE was prepared by carefully selecting two FRs with significant difference in their solvation abilities. As expected, the unique solvation structure of LHCE is achieved for the DFR electrolytes and effective SEIs were formed on Gr electrodes. Consequently, Gr||LFP cells using the DFR electrolytes achieved comparable cycle life to the conventional electrolyte in the cycling performance. However, contrary to the conventional understanding, the rigorously non-flammable electrolytes do not outperform the baseline electrolyte in safety performance evaluations on the battery level. 18650 type Gr||LFP batteries using DFR-E suffer from cell rupture in the nail penetration and overheating tests. The operando temperature record suggests that DFR-E reacts with charged electrode materials under abusive conditions. Comparative DSC measurements further identify that TMPa is the culprit behind the inferior safety performance of the cells using DFR-E.

The work reveals a sobering message that the non-flammability of the electrolyte is not-the key parameter associated with an enhanced safety performance on a cell level. Among the factors that influence the safety performance of LIBs, the reactivity between the electrolyte and the charged electrodes, overweighs the flammability of the bulk electrolyte. The safety performance of certain non-flammable electrolytes needs to be revaluated (especially those contain large amounts of organic phosphate solvents). For future safe electrolyte development, it should be kept in mind that achieving non-flammability on the electrolyte is only the starting point rather than the finishing line of enhancing the safety properties of LIBs. The safety evaluations on a cell level or even a battery level, such as overheating, overcharging, nail penetration, must be performed.

Acknowledgments

1.0 Introduction

Because of their merits of high energy density, long cycle life, excellent energy efficiency, lithium (Li)-ion batteries (LIBs) have become an indispensable device in our daily lives. They can be found in devices such as smart phones, laptops, drones, electric vehicles, and stationary power stations. Because of the ubiquity of LIBs, the poor safety performance of LIBs under abusive conditions has become a major concern. The electrolytes used in the state-of-the-art commercially available LIBs are considered as one of the causes for the safety hazard of LIBs. These electrolytes are usually comprised of 1.0-1.2 M LiPF$_6$ dissolved in a mixture of ethylene carbonate (EC) and other linear/cyclic organocabonates (hereinafter, conventional electrolytes). Due to the flammability of organocarbonate solvents, the conventional electrolytes exhibit relatively high flammability, which was considered as one of the major culprits of the safety hazard of LIBs. In the aim of enhancing the safety performance of LIBs, tremendous efforts have been devoted in suppressing the flammability of the electrolytes. Because of their flame retarding effects, phosphorus (P)-based flame retardants (FRs), such as trimethyl phosphate (TMPa)[1], triethyl phosphate (TEPa)[2], tris(2,2,2-trifluoroethyl) phosphite (TTFEPi)[3], dimethyl methyl phosphonate (DMMP)[4], pentafluoro (phenoxy) cyclotriphosphazene (FPPN)[5], triethoxyphosphazen-N-phosphoryldiethylester (PNP)[6] have long been considered as the key to improving the safety performance of LIBs.[1, 7] However, the direct introduction of an FR into the conventional LiPF6-organocarbonate electrolytes usually leads to significantly deteriorated electrochemical performance of the LIBs, because of its interference to the formation of solid electrolyte interphase (SEI) on graphite (Gr) anodes.[1, 7a, 8] For this reason, the contents of P-based FRs in conventional electrolytes are generally limited since the trade-off between reduced flammability and deteriorated electrochemical performance arises.[8] The emergence of localized high concentration electrolytes (LHCEs) opens a door for increasing the content of FR in the electrolyte because the LHCEs effectively address the incompatibility issue between FRs and negative electrodes.[8-9] In LHCEs, Li cation (Li$^+$), anions and solvating solvents are clustered among the diluent solvent molecules, and the Li salt is poorly dissociated due to the scarcity of the solvating solvent. Because of this unique solvation structure of LHCEs, the anions of Li salt are facilitated to participate in the SEI formation, which resolves the incompatibility issue between P-based FRs and Gr electrodes.[8, 7a, 10] Moreover, because almost all the solvating solvent molecules are coordinated by the Li salt, the anodic stabilities of the electrolytes have been greatly increased since the complexation increases the anodic stability of the solvating solvent.[10a, 11] The key to creating the unique solvation structure of LHCEs lies in the distinctive solvation abilities between the solvating solvent and the diluent. The diluent is expected to have a much weaker solvation ability towards the Li salt than the solvating solvent, so that it barely participates in the complexation with Li salt and the scarcity of solvating solvent is deliberately preserved. Meanwhile, the diluent is required to be miscible with the high concentration electrolytes (HCEs). Because of these rigorous criteria, the state-of-the-art diluents used in LHCEs are predominantly hydrofluoroethers or partially fluorinated ethers, which are both flammable and volatile. For instance, the flash point of one of the most common diluents for LHCEs, 1,1,2,2-tetrafluoroethyl-2,2,3,3-tetrafluoropropyl ether (TTE), is merely 29 ℃.[7a, 10b] In the FR-based LHCEs, the flammability of the bulk electrolyte can be effectively suppressed by the presence of a relatively large amount of the FR, however, the vapors of these LHCEs are still highly flammable. To achieve complete non-flammability, the commonly adopted diluent must be substituted by a non-flammable diluent. Because of its flame-retarding effect and a very low solvating ability towards LiFSI, tris(2,2,2-trifluoroethyl) phosphite (TTFEPi) was selected to substitute the flammable TTE in the LiFSI-TMPa-TTE electrolyte to formulate the completely non-flammable LHCEs of LiFSI-TMPa-TTFEPi.The obtained dual-flame retardant (DFR) electrolytes not only achieved the complete non-

flammability, but also the solvation structure of LHCE. Therefore, they could achieve long-term cycling performance in Gr||LiFePO$_4$ (LFP) cells. Counterintuitively, despite of their non-flammability in both liquid phase and vapor phase, the DFR electrolytes exhibited inferior safety performance than the conventional flammable electrolyte on a battery level. It is revealed that the DFR electrolytes react more violently with both positive and negative electrode materials at charged state than the conventional electrolyte, which is accountable for the inferior safety performance on the battery level. This work delivers a sobering message that, unilaterally reducing the flammability of the electrolyte is far from being adequate to improve safety performance on a battery level. Substantial consideration should also be taken into reducing the reactivity between the electrolyte and the charged electrodes.

2.0 Solvation structure of the DFR electrolytes

TMPa was conventionally considered as an inappropriate solvent for formulating electrolytes used in LIBs, because of its incompetence of forming SEI and, consequently poor compatibility with negative electrodes. However, according to our previous studies, the incompatibility issue with negative electrodes can be probably resolved if it can achieve the unique solvation structure of LCHEs.[7a, 12] The nonpolar, non-flammable diluent TTFEPi was selected to fabricate the completely non-flammable LHCEs. Two DFR electrolytes were prepared: (1) the additive-free electrolyte (DFR-O) with the composition of LiFSI:TMPa:TTFEPi at 1.0:1.4:1.0 by mol. and (2) the EC-containing electrolyte (DFR-E) with the composition of LiFSI:TMPa:EC:TTFEPi at 1.0:1.2:0.2:1.0 by mol. A conventional electrolyte of 1.0 mol L-1 LiPF6 in EC-ethyl methyl carbonate (EMC) at 3:7 by wt. plus 2 wt.% vinylene carbonate (VC) was selected as the baseline electrolyte (hereinafter, E-Baseline). The codes and compositions expressed in molarity were summarized in Table 1.

Table 1. Codes and electrolyte formulae of studied electrolytes

Code	Electrolyte formula
E-Baseline	1.0 M $LiPF_6$/EC-EMC (3:7 by wt.) + 2 wt.% VC
DFR-O	2.1 M LiFSI in TMP_a-$TTFEP_i$ (1.00:1.67 by wt.)
DFR-E	2.1 M LiFSI in TMP_a- EC-$TTFEP_i$ (1.00:0.09:1.67 by wt.)

To obtain a thorough understanding on the microscopic solvation structures of the DFR electrolytes, computational simulations and experimental measurements were performed to elucidate the fine solvation structure of the DFR electrolytes.

To begin with, *ab initio* molecular dynamics (AIMD) simulations on the DFR electrolytes in the presence and absence of EC additive were conducted. Figure 1a exhibits the solvation structures of the DFR-O and DFR-E electrolytes obtained from AIMD. As illustrated, the cations (Li^+), anions (FSI^-), solvating solvent (TMP_a) and additive (if applicable) cling to each other to form the so-called contact ion pairs and aggregates and consequently ion clusters. This is supported by the radial distribution functions (RDFs) obtained from the simulations. As shown in Figure 1b, the Li cations are predominantly coordinated by the oxygen (O) atoms in the TMP_a and FSI^- molecules. The coordination between Li cations and O atoms in TTFEPi is rather weak as only a small peak can be observed at a distance greater than 6 Å. The reason can be assigned to the distinctive solvation abilities between TMP_a/EC and TTFEPi. In DFR-E, a small amount of TMP_a was substituted by EC. Due to the strong affinity between EC and Li^+, EC was also incorporated inside the ion cluster, as indicated in Figure 1b. Due to the high fluorination degree, the electron density of the O atoms in TTFEPi is relatively low, making it less favorable for Li^+ coordination (Figure S1). The AIMD results strongly suggest that the unique solvation structure of LHCEs is formed by TMP_a and $TTFEP_i$.

To better understand the solvation structures of the DFR electrolytes, pulse field gradient nuclear magnetic resonance (PFG NMR) spectroscopy was carried out to evaluate the self-diffusion coefficients of the electrolyte species. As shown in Figure 1c, the self-diffusion coefficients of Li^+, FSI^-, and TMP_a are 2.8, 3.1, and 2.9×10^{-11} m^2 s^{-1}, being very similar to each other. The convergence of the self-diffusion coefficients suggests that these species tend to migrate as an entirety in the electrolyte, due to the strong affinity among these species. In comparison, the self-diffusion coefficient of $TTFEP_i$, 9.8×10^{-11} m^2 s^{-1}, is much higher than the other species since it

barely participates in the coordination with other species. Similar phenomena can be observed in other typical LHCE systems.[7a, 12b, 13] The introduction of EC has negligible influence over the diffusion coefficients of electrolyte species. As illustrated in Figure 1c, self-diffusion coefficients of Li^+, FSI^-, TMP_a and $TTFEP_i$ in DFR-E are 2.6, 2.9, 2.8 and 10.0 × 10^{-11} m^2 s^{-1}, respectively, being almost identical to those in DFR-O. The diffusion coefficient of EC is determined to be 4.0 × 10^{-11} m^2 s^{-1}, which is slightly higher than those of Li^+, FSI^-, TMP_a, suggesting that part of EC exists as free molecules in the electrolyte.
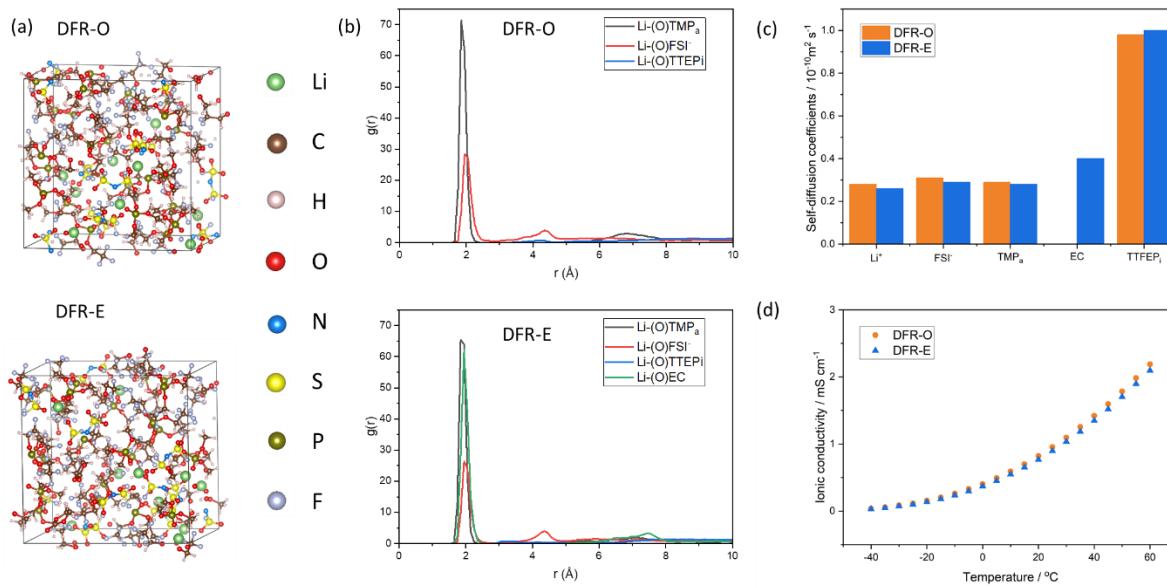

Figure 1. (a) Solvation structures of DFR-O and DFR-E electrolytes obtained by AIMD; (b) RDFs of DRF-O and DFR-E electrolytes obtained from AIMD calculations; (c) self-diffusion coefficients of electrolyte species in DFR-O and DFR-E electrolytes; (d) ionic conductivities of DFR-O and DRR-E electrolytes in the temperature range of -40 to 60 ℃.

With the self-diffusion coefficients of the cation and anion and the measured ionic conductivities (Figure 1d), the dissociation degrees of LiFSI in the DFR-O and DFR-E can be calculated via Nernst-Einstein equation, which are merely 18.6% and 20.3%, respectively. In comparison, the dissociation degree of $LiPF_6$ in E-Baseline is approximately 68% as reported previously, due to the excellent dissociation ability of EC and the excessive amount of solvents.[12b] In the two DFR electrolytes, although TMP_a has the excellent solvation and dissociation abilities due to its relatively high donor number and dielectric constant of 23 and 20.6, respectively,[14] the relative scarcity of TMP_a to LiFSI impedes the dissociation of LiFSI in DFR-O and DFR-E.

Based on the aforementioned evidence, it can be concluded that the difference between TMP_a and $TTFEP_i$ in the Li salt solvation and dissociation has successfully achieved the unique solvation structure of LHCEs, which is characterized by the formation of relatively stable "solvent-ion pairs" or "solvent-ion clusters", as well as the relatively low Li salt dissociation degrees. The addition of a small amount of additive barely changes the solvation structure or the diffusion coefficients of the LHCEs, which is in good agreement with our previous results.[12b]

3.0   Electrochemical performance

3.1   Solvation structure and formation of effective SEI

As reported previously, the incompatibility of TMP_a with Gr anodes can be solved by formulating TMP_a-based LHCEs.[7a] The diluent used in the previous study is TTE, a hydrofluoroether, which has no issue with Gr electrodes. In this study, a partially fluorinated phosphite, $TTFEP_i$, is used as a diluent to formulate the DFR-based LHCEs. Since $TTFEP_i$ does not participate in the solvation structure in the LHCEs, its compatibility with Gr electrode is unknown. To verify this, Li||Gr cells comprising the two DFR-based electrolytes and the E-Baseline were assembled.
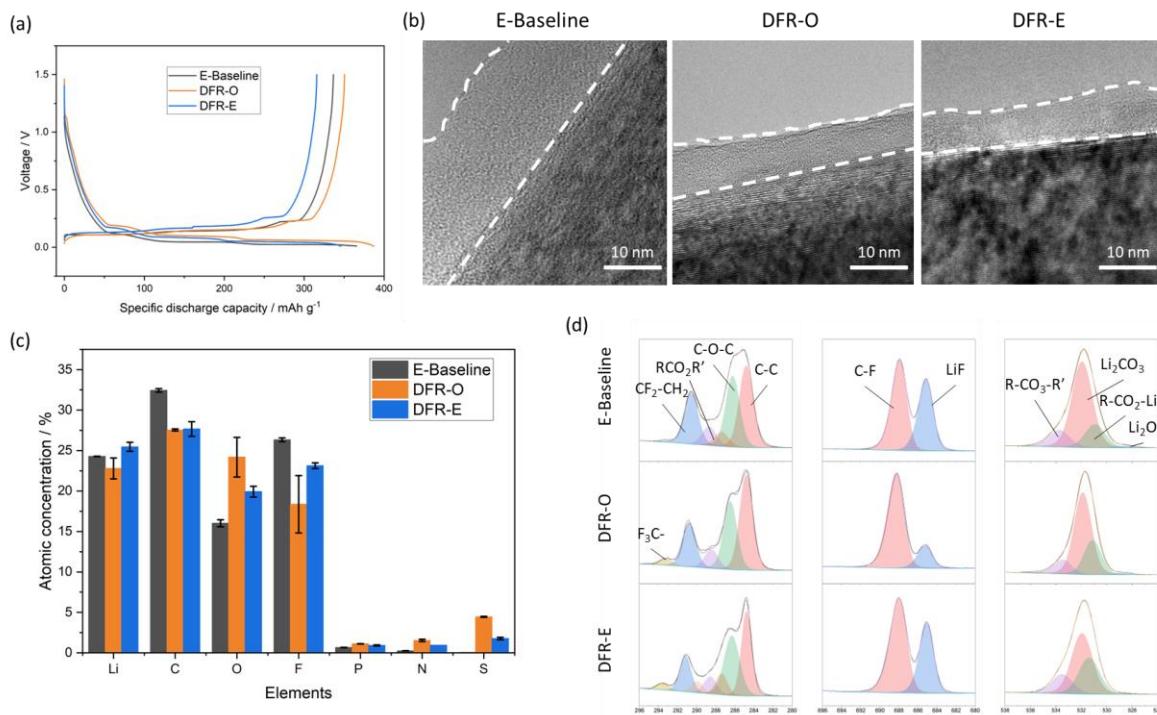

Figure 2. (a) First cycle voltage profiles of Li||Gr half cells using the three electrolytes at C/20 rate. (b) TEM images of SEIs formed in E-Baseline, DFR-O and DFR-E electrolytes after formation cycles; (c) Atomic concentrations of lithium (Li), carbon (C), oxygen (O), fluorine (F), phosphorus (P), nitrogen (N), and sulfur (S) in the SEIs formed in the three studied electrolytes after formation cycles; (d) XPS spectra of C 1s, F 1s and O 1s of the SEIs formed in the three studied electrolytes.

Figure 2a shows the first cycle voltage profiles of Li||Gr half cells using DFR-O, DFR-E and E-Baseline at the charge/discharge rate of C/20. As illustrated in the figure, all the cells achieved reversible lithiation and delithiation, with the Coulombic efficiency (CE) of 92.1%, 90.5 % and 91.3% for DFR-O, DFR-E and E-Baseline, respectively. To further prove that effective SEIs have been formed by the DFR-O and DFR-E electrolytes on Gr electrodes, transmission electron microscopy (TEM) was employed to study the morphologies of the Gr electrodes and the SEIs. As shown in Figure 2b, SEIs were observed in all three Gr samples. In the case of the SEI formed by E-Baseline, the thickness of SEI exceeded 10 nm. In comparison, the thicknesses of SEIs formed by DFR-O and DFR-E were determined to be ≈ 8 nm, being slightly thinner than that formed in E-Baseline. All the SEIs exhibited relatively uniform thickness and highly amorphous

structure. TEM images proved that SEIs are successfully formed by DFR-O and DFR-E electrolytes and the diluent TTFEP$_i$ does not have compatibility issue with Gr electrodes.

The chemical features of the SEIs were studied by X-ray photoelectron spectroscopy (XPS). As shown in Figure 2c, Li, carbon (C), O, fluorine (F) are the most dominant elements in the SEIs formed in the two DFR electrolytes and E-Baseline. In the case of E-Baseline, the atomic concentration of P is 0.66%, being only slightly higher than the detection limit of XPS. Because P is the characteristic element of PF$_6^-$ anion, the low atomic concentration of P in SEI formed by E-Baseline indicates that anions in E-Baseline play a relatively insignificant role in the SEI formation process. In contrast, the atomic concentrations of nitrogen (N) and sulfur (S), being characteristic to LiFSI, amount to 1.53% and 4.45%, respectively in the SEI formed by DFR-O electrolyte. It confirms that the anions in DFR-O take a much more active role in the SEI formation process than those in the E-Baseline, which is consistent with our previous observations.[7a, 12b] The introduction of EC into DFR-O suppressed the anion decomposition (Figure 2c). Nevertheless, the atomic concentrations of N and S in the SEI formed by DFR-E are still significantly higher than that of P in the SEI formed by E-Baseline. It is also worth noting that the P contents in SEIs formed by DFR-O and DFR-E are merely 1.12% and 0.92%, respectively. Because P is characteristic to the solvent (TMP$_a$) and the diluent (TTFEP$_i$) in the DFR electrolytes, it confirms that solvent and the diluent are not actively engaged in the SEI formation process.

Figure 2d exhibits the C 1s, F 1s and O 1s XPS spectra of the SEIs formed in the studied electrolytes. The spectra were fitted according to our previous publications.[7a, 12b] It is revealed that polyethylene oxide-like species (C-O-C), esters, LiF, Li$_2$CO$_3$, oligo/poly organic carbonate (R-CO$_3$-R') are the major common species for all the SEIs. Both DFR-O and DFR-E electrolytes exhibit a small amount of CF$_3$-containing species, which probably originated from the decomposition of S-F bond in the FSI$^-$ anion and reconstruction of C-F bond. Based on the electrochemical, microscopical and spectroscopical evidence, it can be concluded that robust SEIs are formed by DFR-O and DFR-E electrolytes, and FSI$^-$ anions are a major contributor to the SEI formation in the two DFR electrolytes

3.2 Long-term cycling performance evaluation

The unique solvation structure of the DFR electrolytes promoted the formation of effective SEIs on Gr electrodes. However, the formation of an SEI is not a guarantee for good long-term cycling performance of LIBs. To study the applicability of the DFR electrolytes in LIBs, it is imperative to evaluate the long-term cycling performance. For this reason, Gr||LFP cells using E-Baseline and the two DFR electrolytes were assembled and evaluated.

The cells were charged and discharged at the rate of C/20 once and C/10 twice to facilitate the formation of effective SEI on Gr, where 1C = 1.5 mA cm^{-2}. Thereafter, the cells were charged and discharged at C/5 for 300 cycles. After formation cycles, the average specific capacity of Gr||LFP cells using the E-Baseline was determined to be 126.5 mAh g^{-1}, whereas those of DFR-O and DFR-E based cells were 116.5 and 113.6 mAh g^{-1}, respectively, being lower than that of E-Baseline cell (Figure 3a), probably because the two DFR electrolytes have much lower ionic conductivity than E-Baseline, 0.95 mS cm^{-1} (DFR-O) and 0.90 mS cm^{-1} (DFR-E) vs. 8.90 mS cm^{-1} (E-Baseline) at 25 °C, thus the polarization of the cells using DFR electrolytes is higher than that of the E-Baseline cells. It is worth noting that a small amount of the DFR electrolytes was anodically decomposed in the 1st charge/discharge cycle, as two peaks can be observed at ≈3.5 V for Gr||LFP cells using the DFR electrolytes (Figure 3b). It can be probably assigned to the decomposition of the TTFEPi in the electrolytes since it is the most susceptible species toward

anodic decomposition. Nevertheless, such decomposition is self-limiting, as the anodic decomposition peak can no longer be observed in the 2nd cycle (Figure 3c). After 300 charge/discharge cycles, the average specific capacities of Gr||LFP cells using E-Baseline, DFR-O and DFR-E declined to 87.5, 82.8 and 90.8 mAh g^{-1}, corresponding to the capacity retentions of 69.2%, 71.5% and 79.9%, respectively. Cells using both DFR electrolytes exhibited slower capacity decay and higher capacity retention than those using E-Baseline. It is worth noting that although the cells using DFR-E exhibited a lower average initial capacity, their average specific capacity exceeded that of the E-baseline cells after long-term cycling due to the relatively mild capacity decay.
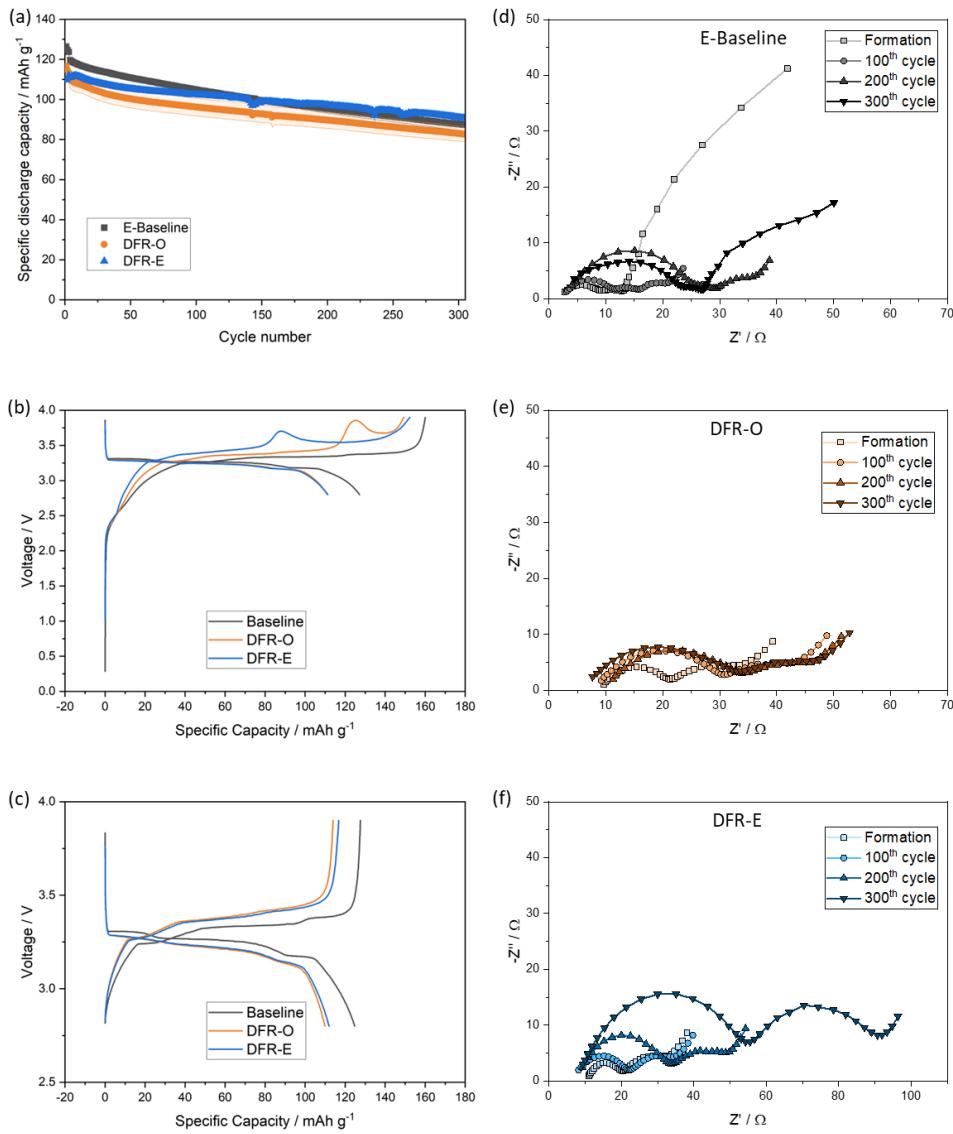
Figure 3. (a) Average specific discharge capacities of Gr||LFP cells using E-Baseline, DFR-O and DFR-E electrolytes cycled within the voltage range of 2.8-3.9 V at C/5 rate under 25.0 ℃ (where 1C = 1.5 mA cm^{-2}). Voltage profiles of Gr||LFP cells in the (b) 1st charge/discharge cycle (C/20) and (c) 2nd charge/discharge cycle (C/10). EIS spectra of the cells at selected cycle numbers for (d) E-Baseline, (e) DFR-O and (f) DFR-E.

Electrochemical performance

To understand the origin of the difference in the capacity decay patterns, electrochemical impedance spectroscopy (EIS) measurement was performed. As illustrated in Figures 3d-3f, E-Baseline cells exhibited smaller values in the bulk electrolyte impedance (R_Ω), SEI impedance (R_{SEI}) and charge transfer impedance (R_{CT}) than the cells using DFR-O and DFR-E after formation cycles. Therefore, Gr||LFP cells using DFR electrolytes exhibited lower initial capacity than the E-Baseline cells. As the cycle number increased, the R_Ω remained almost the same for the cells using all the studied electrolytes. The increase in cell impedance stems mainly from the increase of R_{SEI} and R_{CT}. In the case of E-Baseline, the increase in R_{SEI} and R_{CT} was more significant than that of cells comprising DFR electrolytes. The equivalent circuit and the R_Ω, R_{SEI} and R_{CT} values obtained based on the equivalent circuit were summarized in Supplementary Information (Figure S2). The EIS spectra suggest that the electrode/electrolyte interphases formed in DFR electrolytes are more stable over the long-term cycling performance, which is further confirmed by the post-mortem analyses on SEI and cathode electrolyte interphase (CEI) (Figure S3). It can be concluded that the better capacity retentions of cells using DFR electrolytes originate from their superior electrode/electrolyte interphases formed by these electrolytes.

Electrochemical performance

4.0 Safety features of DFR LHCEs and batteries

After confirming that DFR electrolytes achieved comparable cycle life to the conventional electrolyte in Gr||LFP cells, the safety properties of DFR electrolytes as well as the cells comprising these electrolytes were evaluated.

4.1 Flammability of the electrolytes

Flammability of the electrolytes has long been considered as one of the most influencing factors governing the overall safety performance of LIBs. To verify that the use of FRs as both the solvating solvent and the diluting solvent has significantly suppressed the flammability of the LHCEs, ignition measurements were performed for the electrolytes of DFR-O and DFR-E, along with E-Baseline for comparison. As shown in Figure 4, E-Baseline can be readily ignited by an external ignition source (a butane torch), and the combustion is self-sustained after the removal of the ignition source. In comparison, neither DFR-O nor DFR-E can be ignited (See videos of the ignition tests in Supplementary Information). As expected, DFR electrolytes exhibit excellent resistance towards flame since they are mainly comprised of FRs (TMP$_a$ and TTFEP$_i$).
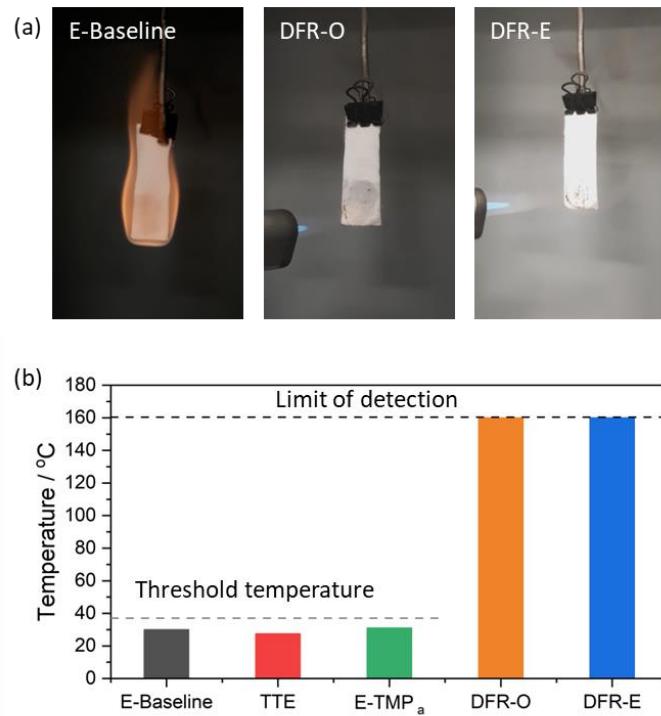
Figure 4. (a) Flammability and (b) flash points of the studied electrolytes determined by ignition tests.

It should be noted that the ignition test emphasizes the flammability of the bulk liquid electrolyte. When being heated during a thermal runaway, the liquid electrolyte vaporizes. At this stage, the volatile solvents in the electrolyte are the dominant species in the vapor phase due to their higher vapor pressures.[15] Therefore, the concentration of the FR in the vapor phase may not be sufficient to fully suppress the flammability of the electrolyte vapor. To prove this point, the flash point of a previously developed LHCE, LiFSI-1.4TMP$_a$-3TTE (by mol., hereinafter, E-TMP$_a$), was evaluated. As shown in Figure 3b, despite the E-TMP$_a$ cannot be ignited in the ignition test,[7a]

the flash point of such electrolyte is merely 31 ℃, being very similar to that of the pure diluent, TTE (29 ℃). It indicates that the flash point of an electrolyte is more dependent on the flash point of the most volatile species. Similarly, the flash point of E-Baseline, the conventional LiPF$_6$-organocarbonate electrolyte is merely 30 ℃, which is approximate to that of pure EMC (23 ℃). Based on the criteria set by the National Fire Protection Association of United States, both E-Baseline and E-TMP$_a$ should be categorized as flammable liquids since their flash points are lower than the threshold value of 37.8 ℃ (100 ℉), although E-TMP$_a$ cannot be ignited at liquid state in the ignition test.

To prove that the DFR electrolytes are non-flammable not only in liquidous state, but also after being vaporized, flash points of DFR electrolytes were evaluated. The flash points of DFR-O and DFR-E exceeded the limit of detection of the flash point determination device (160 ℃). During the measurement, the flames of the device were extinguished by the vapors of both DFR-O and DFR-E. In other words, both the bulk liquid phase and the vapor of DFR-O and DFR-E are flame retarding, because the flammable diluents in the conventional LHCEs were substituted by a flame retarding diluent, TTFEP$_i$.

Based on the flammability and flash point measurements, it can be concluded that both DFR-O and DFR-E exhibit non-flammability in both the liquid phase and the vapor phase. Therefore, they can be categorized as rigorous non-flammable electrolytes.

4.2   Safety performance on cell level

Compared with E-Baseline, DFR electrolytes achieved superior flame resistivity in both liquidous phase and vapor phase. For this reason, they are expected to outperform E-Baseline in safety evaluations on a battery level. To verify this hypothesis, 1.2 Ah 18650 type Gr||LFP batteries were assembled and charged to 3.9 V and 4.0 V, respectively, for which both nail penetration and overheating tests were performed. Because DFR-E achieved a better cycling performance than DFR-O, it is therefore selected for the safety performance evaluation on the cell level.

Figures 5a and 5b summarize the nail penetration results of the 1.2 Ah 18650-type Gr||LFP cells performed under 80 ℃. Counterintuitively, the cell using E-Baseline (Figure 5a) passed the nail penetration test while the DFR-E cell failed (Figure 5b). As shown in Figure 5a, the packaging of the 18650 cells using E-baseline remained almost intact after the nail penetration, except for the nail puncture. After the penetration, the cell temperature merely increased from 80 ℃ to 87 ℃ in the duration of 10 minutes. After a mild voltage decrease in the first few minutes, the voltage of the E-baseline cell stabilized at 3.4 V. In comparison, the DFR-E cell exhibited a significant structural disintegration and severe burn marks. As shown in Figure 5b, the temperature of the cell increased from 80 ℃ to ≈350 ℃ within merely 3 min. After reaching the maximum temperature, the cell started to cool down gradually. Even after 20 min of cooling, the cell temperature was still higher than 150 ℃. The voltage of the cell also exhibited a cliff-like drop that it decreased from 4.0 V to 0 V almost instantaneously after nail penetration, which is probably caused by a complete meltdown of the separator in the cell. Evidently, E-Baseline exhibits superior safety features to DFR-E in the cell level, despite E-Baseline being highly flammable while DFR-E, non-flammable.

Besides the nail penetration tests, overheating tests were also performed for 18650 cells comprising E-Baseline and DFR-E. The cells were heated from ambient temperature to 150 ℃ at a rate of 5 ℃ min^{-1}. In the case of the E-Baseline cell, the temperature of the cell did not show

any sudden increase (Figure 5c). In contrast, an apparent self-heating is observed in the case of DFR-E cell. After the temperature of the cell was heated to 150 ℃, the temperature of the DFR-E cell continued to increase rapidly to more than 210 ℃. After the overheating, the E-baseline cell remained its packaging integrity but the DFR-E cell was ruptured, due to high internal pressure caused by the self-heating reactions.
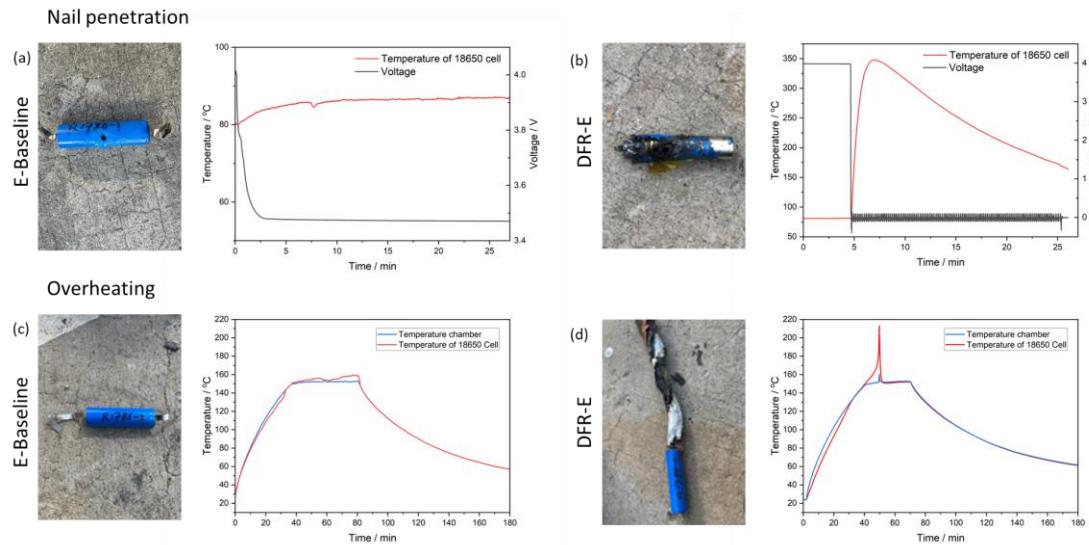

Figure 4. (a) and (b) Photographs (after nail penetration) and temperature/voltage profiles (during nail penetration) of Gr||LFP 18650 cells; (c) and (d) Photographs (after overheating) and temperature profiles (during nail penetration) of Gr||LFP 18650 cells.

Both the nail penetration test and the overheating test reveal that DFR-E is not as safe as E-Baseline on the battery level, although DFR-E exhibits rigorous non-flammability. It is considered that the different behaviors of the 18650 cells in the nail penetration test and the overheating test originated from the different reactivities between the electrolyte and the electrode materials. E-Baseline probably has a very limited exothermic reactivity with both Gr and LFP electrodes and the mild heat release is not sufficient to cause thermal runaway. However, when DFR-E is used, the nail penetration or overheating triggers the violent exothermic reactions between the electrolyte and the electrode(s). The sheer contrast between the complete non-flammability of DFR-E and the violent thermal runaway of DFR-E based cells under abusive conditions emphasizes the fact that non-flammability in electrolyte is far from being a guarantee of achieving enhanced safety performance on a cell level. [16]

4.3 Origin of the inferior safety performance of cells using DFR electrolytes

The question of what caused the more violent exothermic reactions in the cells using DFR-E arises. To discern which component in DFR-E is accountable for the safety hazard, differential scanning calorimetry (DSC) was employed to study different interactions between the DFR-E electrolyte and the Gr or LFP electrodes. Two additional electrolytes, 1 mol LiFSI in EC-EMC (3:7 by wt.) with 2 wt.% VC (noted as E-Baseline-2, an analog to E-Baseline) and LiFSI-1.4TMP$_a$ (by mol., or 3.4 mol L^{-1} LiFSI in TMP$_a$, noted as FR-HCE) were prepared as additional references.

Figure 6a illustrates heat flow of lithiated Gr (charged to 3.9 V) with the electrolytes. In the case of E-Baseline, a weak exothermic peak at 100 ℃ was observed, and no other exothermic peaks can be observed. After substituting LiPF$_6$ with LiFSI (E-Baseline-2), the exothermic at 100 ℃ vanished, indicating that the exothermic reaction between E-Baseline and lithiated Gr originates from LiPF$_6$.[17] In the case of E-Baseline-2, a doublet exothermic peak can be observed in the temperature range of 180-225 ℃, which apparently originates the interaction between LiFSI and lithiated Gr electrode. In the case of FR-HCE, a relatively wide and mild exothermic peak can be observed at the temperature range of 90-140 ℃ and a strong peak can be observed at ≈225 ℃, both of which should be assigned to the reactions between TMP$_a$ and lithiated Gr.
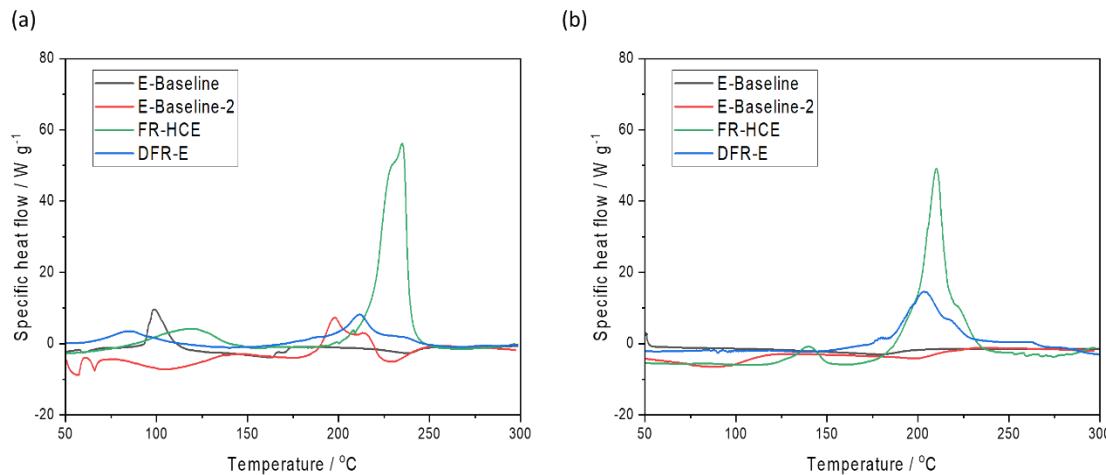

Figure 6. Heat flow of (a) lithiated Gr electrode and (b) delithiated LFP electrode in the presence of the formulated electrolytes. (Obtained with DSC with the temperature increase rate of 10 ℃ min^{-1}).

Besides the reaction between the electrolyte and the lithiated Gr, the reactivity between the electrolytes and the delithiated LFP electrode is also considered. Figure 6b illustrates heat flow of delithiated LFP (charged to 3.9 V) with the electrolytes. As shown in the graph, there are no exothermic reactions between LFP and E-Baseline in the entire temperature range. After substituting the conduction salt in the E-Baseline (*i.e.*, LiPF$_6$) by LiFSI (red curve), no exothermic reactions can be observed either, indicating that LiFSI in DFR-E is not the cause. In comparison, strong exothermic reactions between the FR-HCE and LFP can be observed. At ≈140 ℃, the exothermic reaction is relatively mild, however, the exothermic reaction at ≈200 ℃ is much more violent. Since LiFSI does not react with LFP, it suggests that TMP$_a$ is the major culprit for the exothermic reaction. Compared with the FR-HCE, DFR-E has a lower TMP$_a$ concentration. Consequently, the reaction between DFR-E and LFP is milder than that between FR-HCE and LFP.

Based on the above evidence, it can be concluded that the phosphate solvents, e.g. TMP$_a$ in this work, are actually the major cause for the exothermal reactions with both electrodes. In spite of its flame retarding effect, the immense heat release caused by TMP$_a$ leads to the thermal runaway of LIBs, which consequently makes the cells unsafe.

5.0 Experimental Section/Methods

Electrolyte preparation: A conventional $LiPF_6$-organic carbonate electrolyte, 1.0 mol L^{-1} $LiPF_6$ in EC-EMC (3:7 by wt.) + 2 wt.% VC was employed as the benchmark electrolyte. The non-flammable LHCEs based on two FRs were prepared in a stepwise manner: (1) LiFSI was first dissolved into TMP_a or TMP_a-EC at a molar ratio of 1.0 : 1.4 for LiFSI : TMP_a or 1.0 : 1.2 : 0.2 for LiFSI : TMP_a : EC to yield TMP_a based HCEs, and (2) the HCEs were diluted with $TTFEP_i$ (equivalent to the mole of LiFSI) to yield the dual flame retardant (DFR) LHCEs.

Assembly of Gr||LFP coin cells: Laminates of Gr and LFP electrodes were obtained from the Cell Analysis, Modeling, and Prototyping (CAMP) Facility at Argonne National Laboratory (ANL) and their corresponding areal capacities were 1.8 and 1.5 mAh cm^{-2}, respectively. Electrode disks of Gr (15.0 mm in diameter) and LFP (12.7 mm in diameter) were punched, dried at 110 °C under vacuum for at least 12 h, and subsequently transferred into an argon-filled glovebox (MBraun, H_2O < 0.1 ppm, O_2 < 0.1 ppm). CR2032 coin cell kits were ordered from MTI Corporation. Each coin cell was assembled with a piece of LP disk, a piece of polyethylene separator (Asahi Hi-Pore, Japan), a piece of Gr disk, and 50 μL of the electrolyte. To avoid the anodic corrosion of stainless steel in LHCEs at high voltages, the aluminum (Al)-clad positive case was employed and an additional Al foil of 19.0 mm diameter was placed in between the positive cathode disk and the Al-clad positive case during the cell assembly.

Assembly of Gr||LFP 18650 cylindrical cells: Gr||LFP 18650 cells with about 1.2 Ah capacity were made according to American Lithium Energy (ALE)'s standard procedures using the commercial 18650 cell parts. Specifically, the LFP electrode was made through mixing conductive carbon additive with 8% PVDF in NMP solution followed by the addition of LFP powder to yield the electrode paste. Subsequently, the LFP electrode paste was coated to 16 μm Al foil using a fully automatic coma coater, which was dried and calendered to LFP electrode sheets. The Gr negative electrode was made through by dispersing Gr with dissolved 2% CMC aqueous solution. SBR was introduced into the slurry to yield the Gr electrode paste, which was coated onto 8 μm Cu foil, dried and calendered to the target thickness. After the electrodes were made, they were wound to a jellyroll using the semi-automatic winder. Then the jellyroll was inserted to the can and dried. The dried cells were filled with the electrolyte and then sealed through the crimping. The 18650 cells were conducted formation cycles after 24 h aging at room temperature.

Cycling performance evaluation of Gr||LFP coin cells: After cell assembly, the coin cells were placed in a temperature chamber (TestEquity TEC1) of 25 ± 0.1 °C, connected to a LAND battery testing system (CT2001A) and rested for 12 h. After resting, the cells were charged/discharged at the rate of C/20 once and the rate of C/10 twice to facilitate a complete formation of SEI. After the formation cycles, the Gr||LFP cells were charged at C/5 and discharged at C/3 for 300 cycles. The voltage range was set as 2.8-3.9 V for all the cells.

Electrochemical impedance spectroscopy (EIS) of Gr||LFP coin cells: After every 100 cycles, one of the parallel cells was disconnected from the battery tester for the EIS measurements at fully charged state under 25.0 °C. The perturbation signal ranged from 10^5-10^{-1} Hz at an amplitude of 10 mV.

Ignition test and flash point measurement: The flammability of the studied bulk electrolytes was determined by the direct ignition test. The procedure was kept the same as that described in our previous publications. 2 mL of electrolyte sample was loaded to a glass fiber separator

(Whatman® glass microfiber filters, Grade GF/D). The sample was ignited by a butane torch for 1 s and the butane torch was removed and the flammability of the electrolytes was recorded by an optical video camera.

A semiautomatic flash point tester, Rapid Tester Model RT-1 (ERDCO Engineering Corporation, Evanston, IL), was used for determining the flash points of the studied electrolytes. The measurements followed a closed cup type equilibrium procedure that meets the exact dimensional requirements of domestic and international standards. The sample was injected into the testing cup and heated to a starting temperature. After the sample reached the designated starting temperature, the shutter of the cup was opened, and the vapor of the sample was exposed to an open flame source above the cup for 2 seconds. If the vapor could not be ignited at the starting temperature, the temperature of the sample was consecutively increased by 5 °C/step until flashing was observed. Otherwise, the temperature was consecutively decreased by 5 °C/step until flashing could not be observed. The critical temperatures were recorded and employed as the starting temperature for final determination of the flash points. The heat-search process was repeated at a temperature interval of 1 °C to obtain the accurate flash point of the sample while a fresh sample was used at each step with a temperature change.

Nail penetration test on Gr||LFP 18650 cells: A steel nail with the diameter of 3 mm was employed to puncture the 18650 cells. The speed of the nail was controlled at approximately 30 mm s^{-1}. After the nail penetrated the cell, the nail stayed in the cell for 30 min. The temperature and the voltage of the cell were measured with a thermal couple and a voltage meter during the entire measurement.

Overheating test on Gr||LFP 18650 cells: Being connected to a thermal couple and a voltage meter, the 18650 cells were placed into a temperature chamber. The temperature of the chamber increased from ambient temperature to 150 ℃ at the rate of 5 ℃ min[-1]. Thereafter, the temperature of 150 ℃ was maintained for 30 min, followed by a natural cooling. The temperatures of the cells and the chamber were recorded during the overheating test.

Differential scanning calorimetry (DSC) of electrodes in the presence of electrolytes: A DSC-Q20 was employed to perform the DSC measurements. After formation cycles, the coin cells were fully charged to 3.9 V. At the fully charged state, both LFP (delithiated) and Gr (lithiated) electrodes were retrieved from the cell. After removing the salt residue with excessive amount of solvent, the electrode disks were dried, and the electrode materials were ablated from the current collectors mechanically. The collected electrode material powers were weighed in pans, and 10 μL of electrolyte was introduced into each pan. The pans were sealed and transferred to the DSC-Q20 device. The temperature increased from 40 ℃ to 300 ℃ at the rate of 10 ℃ min[-1] under N_2 flow. The heat flow was calculated by using the mass of electrode material power as the denominator.

Ab initio molecular dynamic simulations (AIMD): To elucidate the solvation structure of DFR electrolytes, AIMD simulations were performed with VASP (Vienna Ab initio Simulation Package) as per the procedure described in our previous publications.[7a, 12b, 18] Stoichiometric LiFSI, TMP_a, $TTFEP_i$ and additive (if applicable) were randomly placed in a unit cube according to the gravimetric densities of the electrolytes. Molecular mechanics was performed for the space unit to obtaining the initial optimized geometry structures, on which AIMD simulations were performed. After 5 ps of pre-equilibration simulation, production simulations were conducted with a time step of 1 fs to the total production time of 10 ps.

Pulsed-field gradient nuclear magnetic resonance (PFG-NMR): An Agilent DD2 500 spectrometer coupled with a 5 mm HX z gradient OneNMRprobe was employed to perform the PFG-NMR experiments. Larmor frequencies of 499.97, 470.39 and 194.32 MHz were used for obtaining the spectra of ^{1}H, ^{19}F, and ^{7}Li, respectively. The self-diffusion coefficients of different electrolyte species were calculated using with the program VnmrJ.

X-ray photoelectron spectroscopy (XPS) of electrodes: The XPS measurements were performed with a Thermo Fisher NEXSA. This system uses a focused monochromatic Al Kα (1468.7 eV) source for excitation with a double-focusing hemispherical analyzer with multi-element input lens and 128 channel detector. The X-ray beam is incident to normal to the sample and the photoelectron detector is 60° off normal. High-energy resolution spectra were collected using a pass-energy of 50 eV with a step size of 0.1 eV and a dwell time of 50 ms. The full-width-at-half-maximum (FWHM) was measured to be 0.82 eV for the Cu 2p3/2 peak using the same conditions as those at which the narrow scan spectra were collected.

Transmission electron microscopy (TEM) of electrodes: The morphologies of SEIs on Gr particles and the structures of LFP were characterized by a 300 kV FEI Titan monochromated (scanning) transmission electron microscope ((S)TEM) equipped with a probe aberration corrector. The Gr particles were mechanically removed from the electrode disk by applying a blade to the retrieved electrodes. The Gr particles removed from the electrode were collected by a Cu TEM grid. The LFP particle samples were prepared by focused ion beam (FIB) sputtering. Detailed procedures were included in our previous publication.[12b] The obtained LFP TEM samples were characterized.

6.0 References

[1] X. Yao, S. Xie, C. Chen, Q. Wang, J. Sun, Y. Li, S. Lu, Journal of power sources 2005, 144, 170.

[2] L. Jiang, C. Liang, H. Li, Q. Wang, J. Sun, ACS Applied Energy Materials 2020, 3, 1719.

[3] S. Zhang, K. Xu, T. Jow, Journal of Power Sources 2003, 113, 166.

[4] H. Xiang, H. Xu, Z. Wang, C. Chen, Journal of Power Sources 2007, 173, 562.

[5] T. Dagger, C. Lürenbaum, F. M. Schappacher, M. Winter, Journal of Power Sources 2017, 342, 266.

[6] B. Wu, F. Pei, Y. Wu, R. Mao, X. Ai, H. Yang, Y. Cao, Journal of Power Sources 2013, 227, 106.

[7] a) H. Jia, Y. Xu, X. Zhang, S. D. Burton, P. Gao, B. E. Matthews, M. H. Engelhard, K. S. Han, L. Zhong, C. Wang, W. Xu, Angewandte Chemie International Edition 2021, 60, 12999; b) X. Wang, E. Yasukawa, S. Kasuya, Journal of The Electrochemical Society 2001, 148, A1058.

[8] H. Jia, W. Xu, Current Opinion in Electrochemistry 2021, 30, 100781.

[9] a) Y. Yamada, J. Wang, S. Ko, E. Watanabe, A. Yamada, Nature Energy 2019, 4, 269; b) Z. Zeng, V. Murugesan, K. S. Han, X. Jiang, Y. Cao, L. Xiao, X. Ai, H. Yang, J.-G. Zhang, M. L. Sushko, J. Liu, Nature Energy 2018, 3, 674; c) L. Tan, S. Chen, Y. Chen, J. Fan, D. Ruan, Q. Nian, L. Chen, S. Jiao, X. Ren, Angewandte Chemie International Edition 2022, e202203693; e) J. Wang, Y. Yamada, K. Sodeyama, E. Watanabe, K. Takada, Y. Tateyama, A. Yamada, Nature Energy 2018, 3, 22.

[10] a) H. Wu, H. Jia, C. Wang, J. G. Zhang, W. Xu, Advanced Energy Materials 2021, 11, 2003092; b) X. Cao, Y. Xu, L. Zhang, M. H. Engelhard, L. Zhong, X. Ren, H. Jia, B. Liu, C. Niu, B. E. Matthews, H. Wu, B. W. Arey, C. Wang, J.-G. Zhang, W. Xu, ACS Energy Letters 2019, 4, 2529.

[11] L. Suo, O. Borodin, T. Gao, M. Olguin, J. Ho, X. Fan, C. Luo, C. Wang, K. Xu, Science 2015, 350, 938.

[12] a) X. Cao, H. Jia, W. Xu, J.-G. Zhang, Journal of the Electrochemical Society 2021, 168, 010522; b) H. Jia, Y. Xu, S. D. Burton, P. Gao, X. Zhang, B. E. Matthews, M. H. Engelhard, L. Zhong, M. E. Bowden, B. Xiao, K. S. Han, C. Wang, W. Xu, ACS Applied Materials & Interfaces 2020, 12, 54893.

[13] T. Tamura, K. Yoshida, T. Hachida, M. Tsuchiya, M. Nakamura, Y. Kazue, N. Tachikawa, K. Dokko, M. Watanabe, Chemistry letters 2010, 39, 753.

[14] R. Schmid, Journal of Solution Chemistry 1983, 12, 135.

[15] P. Atkins, P. W. Atkins, J. de Paula, Atkins' Physical Chemistry, Oxford University press, 2014.

[16] a) X. Liu, L. Yin, D. Ren, L. Wang, Y. Ren, W. Xu, S. Lapidus, H. Wang, X. He, Z. Chen, Nature Communications 2021, 12, 1; b) Y. Wu, D. Ren, X. Liu, G. L. Xu, X. Feng, Y. Zheng, Y. Li, M. Yang, Y. Peng, X. Han, L. Wang, Z. Chen, Y. Ren, L. Lu, X. He, J. Chen, K. Amine, M. Ouyang, Advanced Energy Materials 2021, 11, 2102299; c) Y. Wu, X. Liu, L. Wang, X. Feng, D. Ren, Y. Li, X. Rui, Y. Wang, X. Han, G.-L. Xu, H. Wang, L. Lu, X. He, K. Amine, M. Ouyang, Energy Storage Materials 2021, 37, 77; d) H. Jia, H. Onishi, N. von Aspern, U. Rodehorst, K. Rudolf, B. Billmann, R. Wagner, M. Winter, I. Cekic-Laskovic, Journal of Power Sources 2018, 397, 343.

[17] H. Jia, H. Onishi, R. Wagner, M. Winter, I. Cekic-Laskovic, ACS applied materials & interfaces 2018, 10, 42348.

[18] a) H. Jia, X. Zhang, Y. Xu, L. Zou, J.-M. Kim, P. Gao, M. H. Engelhard, Q. Li, C. Niu, B. E. Matthews, T. L. Lemmon, J. Hu, C. Wang, W. Xu, ACS Applied Materials & Interfaces 2021, 13, 44339; b) H. Jia, Y. Xu, L. Zou, P. Gao, X. Zhang, B. Taing, B. E. Matthews, M. H.

Engelhard, S. D. Burton, K. S. Han, L. Zhong, C. Wang, W. Xu, Journal of Power Sources 2022, 527, 231171.

Appendix A – Supporting Information

1. Charge density of TMP$_a$ and TTFEP$_i$

The charge densities of trimethyl phosphate (TMP$_a$) and tris(2,2,2-trifluoroethyl) phosphite (TTFEP$_i$) were calculated by density functional theory (DFT) calculations, which were performed using the B3LYP functional with the NWChem software. The geometries of molecules were optimized with 6-31G** basis. Long-range dispersion interaction was corrected by Grimme's DFT-D3 method. Single point energy calculations were performed using 6-311++G(d,p) basis set. Vibrational frequencies were calculated for yielding zero-point energy and thermal corrections. Gibbs free energies were calculated at 298.15 K. The electrostatic potential surfaces were visualized by visual molecular dynamics (VMD) program.

As shown in Figure S1, the central oxygen atom in TMP$_a$ exhibits a very high charge density. Therefore, it is a favorable site for the coordination between TMP$_a$ and Li ion. The charge density of the central phosphorus (P) atom in TTFEP$_i$ is much lower than that of the central oxygen (O) atom of TMP$_a$, making it less favorable for coordination toward Li ions. In TTFEPi, O atoms between P and CH$_2$CF$_3$ group have the highest charge density. However, due to the electron withdrawing effect of the CF$_3$ group, the coordination ability of TTFEP$_i$ is much lower than that of TMP$_a$.

TMP$_a$ TTFEP$_i$
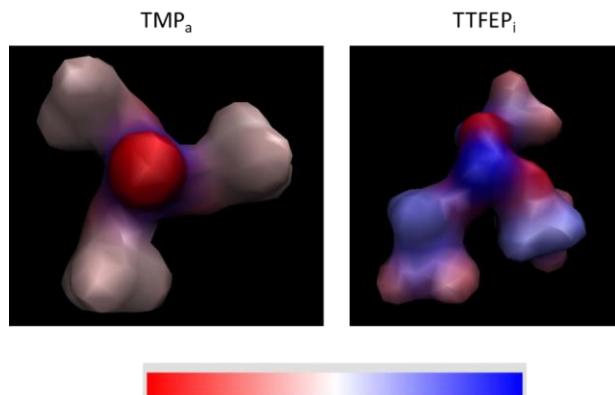
Figure S1.   Distribution of electron density in TMP$_a$ and TTFEP$_i$ determined by DFT calculations.

2. Fitting of the Nyquist Plot

The Nyquist plots of the data were fitted by Zview with the following equivalent circuit shown in Figure S2, where R1=R$_\Omega$, R2=R$_{SEI}$, R3=R$_{CT}$, CPE stands for constant phase element, which is used to represent the electric double layer, and Ws is Warburg impedance, which is introduced to represent ion diffusion inside electrode.
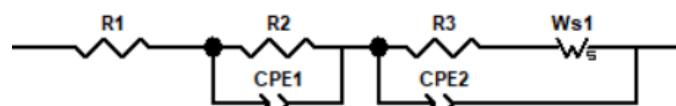

Figure S2.   Equivalent circuit of lithium-ion battery used for the fitting of electrochemical impedance spectra.

Based on the equivalent circuit and the Nyquist plots, R_Ω, R_{SEI} and R_{CT} were extracted and the results were summarized in Table S1.

Table S2. Impedances of Gr||LFP coin cells after 300 charge/discharge cycles obtained by data fitting.

	Cycle number	R_Ω	R_{SEI}	R_{CT}
E-Baseline	Formation	1.5	5.5	9.7
	100 cycles	1.5	7.5	8.5
	200 cycles	1.9	19.4	9.3
	300 cycles	1.1	23.4	9.8
DFR-O	Formation	9.3	10.5	25.0
	100 cycles	8.3	20.7	26.8
	200 cycles	9.9	23.5	16.9
	300 cycles	6.1	23.9	33.7
DFR-E	Formation	10.6	8.8	24.8
	100 cycles	6.8	14.5	22.0
	200 cycles	7.8	24.8	21.8
	300 cycles	7.8	48.2	33.8

R_Ω represents the ohmic resistance of the cell. Since the DFR electrolytes have much lower ionic conductivities than the E-Baseline, the R_Ω values of these cells are significantly larger than that of the E-Baseline cells. In all cells, the increase of R_{SEI} is the biggest contributor to the overall impedance increase.

3. Morphologies of SEI and CEI formed in studied electrolytes after long-term cycling performance evaluation

Figure S3 compares the morphologies of SEIs on Gr and CEIs on LFP after long-term cycling performance evaluation. As shown in Figure S3a, the thickness of SEI of E-Baseline ranges from 15 to 32 nm, which is significantly thicker than those of DFR-O and DFR-E (Figures S3b and S3c). However, it is also worth noting that some graphene layers can be observed in the DFR electrolytes. It indicates that some mild graphite exfoliation took place over the long-term cycling. Nevertheless, most part of the Gr particles maintained structural integrity, indicating the effectiveness of SEI formed by the DFR electrolytes.

Figures S3d-3f exhibits the morphologies of the LFP electrodes after the cycling performance evaluations. In the samples, a "sandwich" structure can be observed, which is comprised of a highly crystalline LFP phase, an amorphous CEI phase and a polycrystalline phase of Pt. The CEI in E-Baseline is slightly thicker than those in DFR-E and DFR-O electrolytes. Despite that the DFR electrolytes decompose on LFP electrodes in the formation cycles (as indicated by Figure 3b), the relatively thin CEI after long-term cycling performance evaluation proves that the

CEIs formed by the DFR electrolytes are temporally stable, which contributes to the relatively high-capacity retentions of the DFR LIBs.
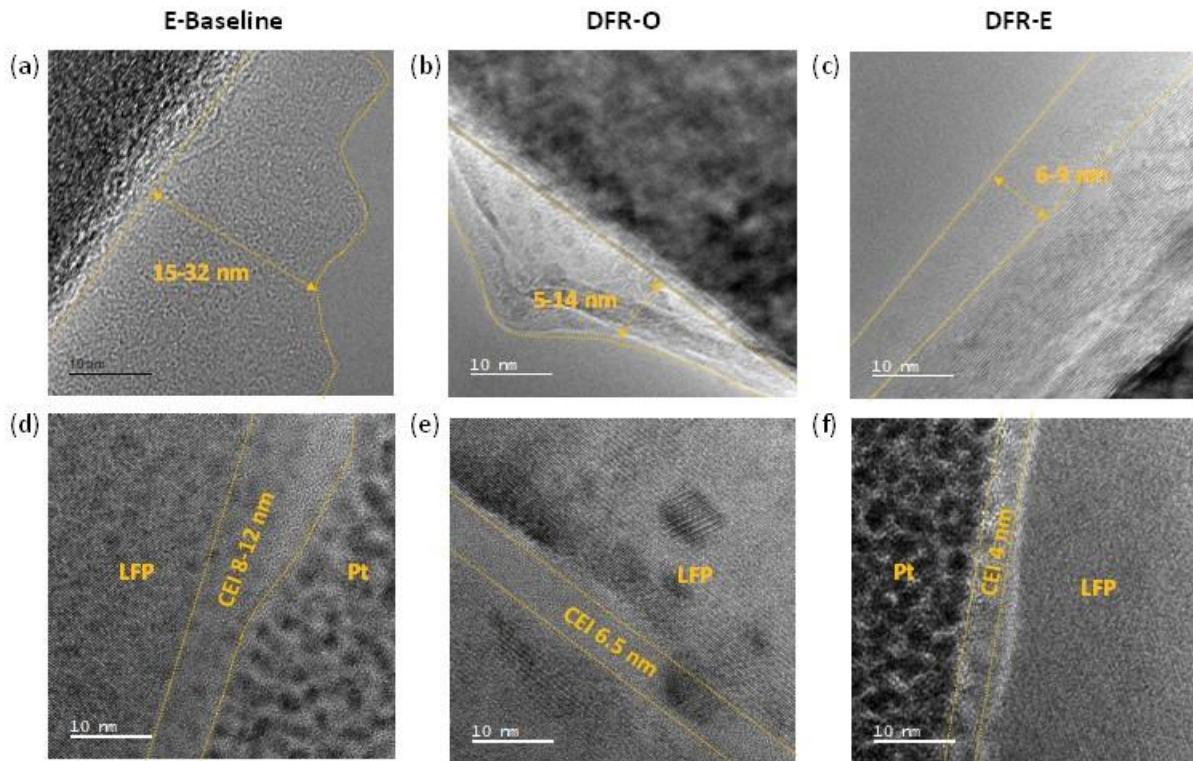

Figure S3.   Morphologies of SEIs on Gr formed in (a) E-Baseline, (b) DFR-O and (c) DFR-E, determined by transmission electron microscopy (TEM) after 300 charge/discharge cycles; Morphologies of CEIs in LFP formed in (d) E-Baseline (e), DFR-O and (f) DFR-E determined by TEM after 300 charge/discharge cycles. Note: During sample preparation of LFP slices for TEM characterization, a Pt protection layer was redeposited on the surface of LFP particle so Pt was detected.

Pacific Northwest National Laboratory

902 Battelle Boulevard
P.O. Box 999
Richland, WA 99354

1-888-375-PNNL (7665)

www.pnnl.gov